Carbon 231 (2025) 119687

Contents lists available at ScienceDirect

Carbon

journal homepage: www.elsevier.com/locate/carbon

Research paper

# Predicting graphene production with population balance modelling

Diego T. Perez-Alvarez [a], Sofia Marchesini [b], Keith R. Paton [b], Jack Sykes [d,c], Dawid Hampel [d], Jennifer Burt [e], Konstantinos Despotelis [b], Diogo Fernandes [e], Philip Davies [a], Christopher Windows-Yule [c,d], Tzany Kokalova Wheldon [d], Andrew J. Pollard [b], Jason Stafford [a,*]

[a] *School of Engineering, University of Birmingham, Edgbaston, Birmingham, B15 2TT, United Kingdom*
[b] *National Physical Laboratory, Hampton Road, Teddington, TW11 0LW, United Kingdom*
[c] *School of Chemical Engineering, University of Birmingham, Edgbaston, Birmingham, B15 2TT, United Kingdom*
[d] *School of Physics and Astronomy, University of Birmingham, Edgbaston, Birmingham, B15 2TT, United Kingdom*
[e] *Malvern Panalytical, Grovewood Road, Malvern, WR14 1XZ, United Kingdom*

## ARTICLE INFO

*Keywords:*
Graphene
Graphite
Exfoliation
Top-down
Synthesis

## ABSTRACT

For sustainable production and industrial adoption of graphene and related two-dimensional materials, an important factor that has yet to be addressed is the ability to forecast material production under specific operating conditions. In this study, by monitoring changes in the distribution of graphite particles as they undergo breakup in a top-down liquid-phase exfoliation process, we show that statistical population balance models (PBM) are a feasible and effective solution for establishing yield and future production of graphene nanosheets, as well as other quantities of interest such as graphene nanoplatelets. A combination of laser diffraction and few-layer graphene concentration measurements are used to recover the material distribution and fit the PBM over all scales respectively. This fitted PBM can then be used to examine production over time, or coupled with nuclear magnetic resonance proton relaxation measurements to recover surface area scaling with particle size. Furthermore, to examine the dynamic process conditions inside the vessel, radioactively labelled graphite flakes and density-matched glass beads functioned as tracer particles for positron emission particle tracking during synthesis. This Lagrangian particle tracking technique can reconstruct the position of the tracer temporally, allowing for ergodic measurements of averaged quantities inside the exfoliating system. Collectively, these results and models provide insights on the breakage mechanisms and fluid dynamics that underpin exfoliation processes for two-dimensional materials, and provide direction for the intensification and optimisation of synthesis processes.

## 1. Introduction

Graphene and related two-dimensional materials (2DMs) have garnered substantial attention since their extraordinary properties and mechanical isolation were demonstrated by Novoselov et al. [1]. Although these materials and their larger stacked counterparts (nanoplatelets) are making their way into diverse applications including construction [2], environmental remediation [3], and energy storage [4], the challenge of efficient and controlled large-scale synthesis persists. Key issues revolve around scaling production of 2DMs without introducing structural defects which would hinder their performance, maintaining material quality control of processes, and optimising process yields for energy and resource efficiency. Presently, manufacturing technologies are classified into two categories: top-down approaches disassemble a 3D precursor material (such as graphite for graphene), whereas bottom-up methods directly synthesise 2DMs from their atomic foundations. It has been shown that industry can produce material at scale using top-down processes [5], which involve applying an external force to break apart the layered material into smaller particles, and eventually nanomaterial. Numerous techniques exist to break these materials, encompassing chemical [6], electrochemical [7] or mechanical [8] methods. Above all, mechanical processes warrant consideration as they are generally applicable to all 2DMs, do not significantly alter the chemical structure of the nanomaterial and can be inherently sustainable when avoiding harsh chemicals, oxidising agents and recycling solvent [9,10]. The generality of mechanical processes is exemplified by the original scotch tape method, a form of micro-mechanical cleavage employed by Novoselov et al. [1], where force is directly applied to overcome the van der Waals forces. However, production becomes challenging at scale, as one cannot easily apply forces to all sheets at once without altering the nanomaterial structure. In practice, forces on

---

* Corresponding author.
*E-mail addresses:* DTP587@student.bham.ac.uk (D.T. Perez-Alvarez), j.stafford@bham.ac.uk (J. Stafford).

https://doi.org/10.1016/j.carbon.2024.119687
Received 19 August 2024; Received in revised form 4 October 2024; Accepted 5 October 2024

nanoparticles and particle interactions can alter the size, structure and morphology of the exfoliated material [11]. This juncture represents a critical point in the pursuit of scalable, repeatable, and high-quality 2DM production systems.

Liquid phase exfoliation (LPE) via mechanical force is a low cost and scalable option [12]. This methodology disperses particles in a liquid, where under the exposure of a high shear environment, they break apart into smaller material fragments including nanosheets. The long-term stability of these nanosheets in the exfoliating medium is achieved through the use of appropriate solvents or surfactant additives. The force necessary to produce such an environment can be achieved by a variety of different means, such as through cavitation [13], ultrasonication [14], and turbulence [8]. Intensive shear processes can produce reasonable yields ($\approx$ 10%wt) of few-layer material at the cost of high energy input, material blockages and material quality [15,16]; whereas in milder processes such as Taylor–Couette devices [17], these points are reversed (lower yield, low energy input, avoidance of blockages, and high-quality few-layer material).

Discovering new systems for LPE and scaling their performance from lab to industrial scales is difficult without a description of the underlying breakage processes. Therein, predicting the few-layer material yield achievable through some exfoliation technique ahead of empirical observations can be immensely useful before any financial commitment is made. Such methods to analyse production are still in their infancy. There have been attempts to describe LPE at the nanosheet scale, defining the atomic interactions at which it occurs [11,18,19]. Empirical models can be applied to estimate certain material parameters such as the critical shear rate [8] and material stability [20], with the advantage that it inherently captures the numerous parameters that affect synthesis performance (e.g., precursor quality, Hansen solubility parameters, solvent viscosity, surface tension, etc.). Beyond this, there are no attempts to describe production according to the fluid dynamics present in the process except by ascribing how production scales according to key hydrodynamic parameters of the system [8,17].

The largest non-fluidic effects on the yield are attributed to the dispersing solvent, and careful choice of dispersant is essential [20,21]. Barring this factor, synthesis is predicated by the internal dynamics of the system, where precursor particle breakages occur and directly lead to the production of nanomaterial. This breakage can take multiple different forms, but is dependent on how the process imparts energy to the system. For instance, under cavitating fluid conditions, through high-power probe sonication or jet impingement, precursor particles are shattered and nanosheets can fragment [22]. In the case of 2DMs, this energy can lead to the development of edge defects through the formation of kink bands as sheets separate from the graphite precursor [23]. Less intensive methods, such as LPE in Taylor–Couette cells, produce small quantities of high-quality material through steady attrition of the precursor material [17].

The population balance model (PBM) is a well-established statistical method for exploring the dynamics and relationships of populations applicable to numerous fields. As a system of equations, it defines the dynamics of a population in time and space under a given system and initial conditions. In the study of particle flows, it is a robust and well explored model often applied to evaluate production of aggregates and pharmaceuticals. As the defining trait of LPE is the destruction of precursor particles into their 2DM constituents, there is potential scope for applying PBMs to explore and predict the dynamics of this multi-scale synthesis system. The only prerequisite to applying this type of model is that enough information is collected on the particles in suspension across all scales of interest. An example of a PBM used in this work is given in Fig. 1. The PBM is fitted with only one internal dimension, the particle's volume based diameter $x_v$, and is observed changing in time. Once the PBM is fitted to the PSDs and the dynamics of breakage are known, determining production of any particular size of material over time can then be ascertained simply by integrating over the fraction of interest. Given there are industrial uses for graphene nano-platelet (GNP) ($\gg 10$ atomic layers) and few-layer material ($\leq 10$ atomic layers), this provides several practical advantages for process intensification, quality control, and end-user applications.

In this study, we present a PBM approach to predict the distribution of particles over time for liquid exfoliation of graphite into graphene related nanomaterial. We combine several material characterisation techniques that span from the precursor particle down to the nanomaterial scale, exploring the synthesis space and validating the model. The results show that this pure PBM approach implicitly captures the breakup characteristics of turbulent shear exfoliation processes, offering a method to predict and optimise the mechanochemical synthesis of graphene and related materials. Furthermore, we reveal underlying details about this shear exfoliation process using Raman spectroscopy as well as positron emision particle tracking (PEPT) [25], the latter of which tracks the motion of graphite particles as they move through the system. Collectively, the observations in this work provide insights on the hydrodynamics of mechanochemical synthesis processes for layered materials, and a pathway for predicting material yield performance and important material outputs.

## 2. Methods

### 2.1. Liquid phase exfoliation

A modified kitchen blender (Kenwood BLP31.D0WG, Havant, Hampshire, UK) was used to conduct all LPE experiments (see Fig. 1a). The blender is fitted with a 'jug' vessel, with four blades on the impeller assembly set in opposition to each other, of radius $\sim$ 30 mm. A fixed experimentation volume of 200 mL was maintained throughout. The mixer can reliably maintain stable speeds between $1000 \leq \Omega \leq 18500$ rpm. Modifications to the blender centre around maintaining a stable impeller speed, and an in-depth description of the system and its construction can be found elsewhere [24].

### 2.2. Materials

Graphite (graphite flakes, Sigma Aldrich, St Louis Missouri, product code 332461, CAS number 7782-42-5), with a mesh size +100 (> 149 μm) was chosen as the precursor material and has been used extensively in the literature for LPE studies. Unless otherwise stated, the initial concentration of graphite was 20 mg/mL. An aqueous-surfactant mixture comprising of de-ionised water (200 mL) and sodium cholate (sodium cholate hydrate, Sigma Aldrich, St Louis Missouri, product code C1254, CAS number 206986-87-0) was used as a dispersant for all tests. The concentration was fixed at the critical micelle concentration of 4.3 mg/mL. Sodium cholate is a well documented surfactant in the manufacture of 2DMs, and as a bile extract from natural sources has a low environmental impact (bio-degradable), and is non-toxic at low concentrations [26,27].

As the study investigates particle hydrodynamics and breakup mechanisms, particle-solvent and particle–particle interactions in turbulent flows were examined by comparing with the one-way, two-way and four-way coupled regimes identified by Elghobashi [28]. Graphite dispersions considered in the literature span from low loading (dilute) to dense particulate flows (see the supplementary information). Most analyses in literature place under dilute or moderately dense particle flow interactions, and typically demonstrate precursor material affecting nanomaterial production linearly, i.e. $C \propto C_i$. With a similar system to that used here [29], Varrla et al. [30] demonstrated that under high precursor loading (100 mg/mL) this relationship can break down, suggesting a change in regime where both dense flow and solvent effects may impact yield. Hence, all tests are conducted well below this starting concentration.

In the case of UV-vis-NIR concentration measurements (Section 2.4) and Raman spectroscopy (Section 2.6), exfoliated material was separated from the sediment before analysis. Samples were taken from the

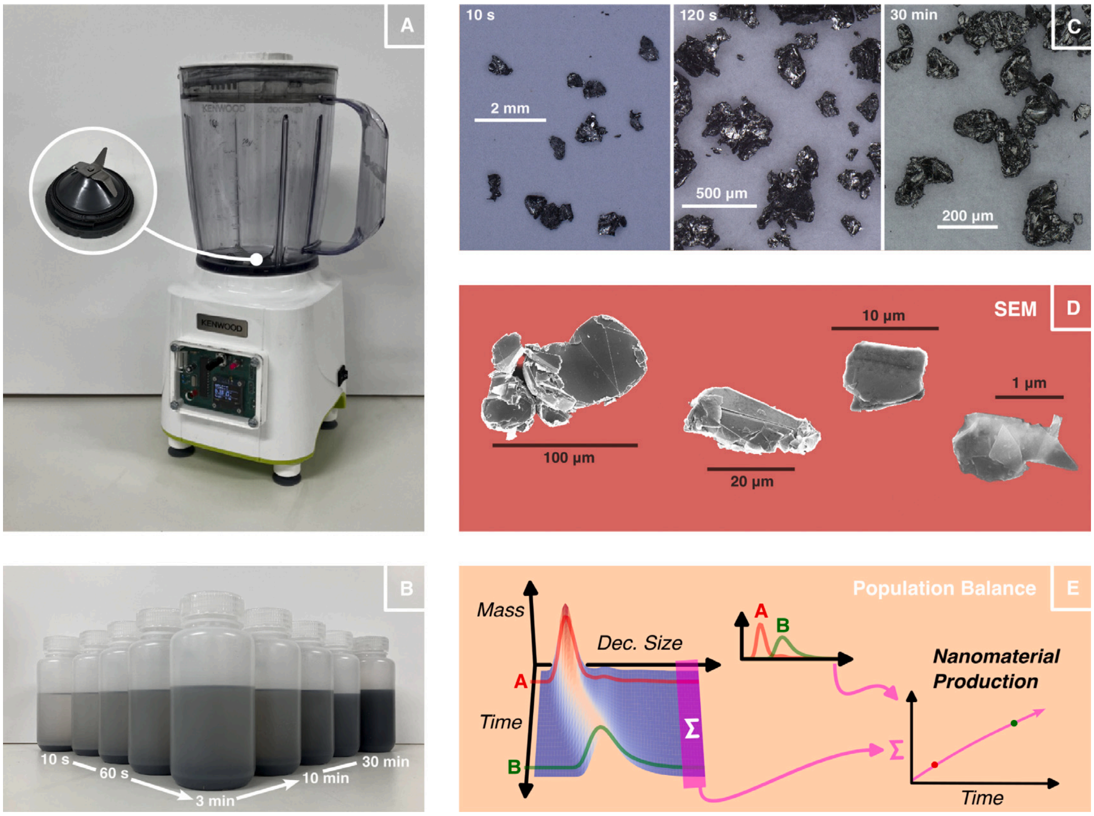

**Fig. 1.** Graphene production and modelling approaches. (A) Impeller-driven blender used in this study, modified for process control [24]. (B) Progression of samples exfoliated from 10 s to 1800 s duration, showing gradual darkening of the graphite/graphene suspensions with time. (C) Optical microscopy of the bulk material at different exfoliation times. (D) Scanning electron microscopy (SEM) images showing the progression of breakage towards smaller particles (all samples analysed were highly polydisperse). (E) Surface plot illustrating the population balance model (PBM) used in this article. An initial distribution of particles (in red) is gradually progressed forwards in time under the influence of a shear exfoliating system. After a period of exfoliation, the original particle size distribution (PSD) gradually transforms as particles are destroyed and birthed into smaller size fractions (in green). Height and colour of the surface indicate the amount of material at the point specified. Summing the mass values of the nano-sizes yields an indication of the amount of nanomaterial produced. (For interpretation of the references to colour in this figure legend, the reader is referred to the web version of this article.)

exfoliation process, placed in 15 mL centrifuge tubes, and centrifuged at 380 relative centrifugal force (RCF) for 45 min, with the top 5 mL of supernatant being recovered for characterisation. The purpose of this centrifugation step was to characterise the few-layer graphene product present within the polydisperse graphitic material in the liquid dispersions.

### 2.3. *Laser diffraction*

A rapid and non-invasive technique, LD measures the angle and intensity of light scattered by particles. Graphitic materials for characterisation by LD were taken directly from the process to ensure homogeneous sampling and measured using Malvern Panalytical Particle Size Analyser Mastersizer 2000 (Malvern, Worcestershire, UK. Fig. 2a). These measurements were used as inputs for the PBM, and were validated against other independent measurements taken using a Malvern Panalytical Particle Size Analyser Mastersizer 3000, with the additional Hydro Insight Dynamic Imaging accessory module. The Hydro Insight module permitted in-line analysis of particle shape and size in tandem to LD measurements. These measurements facilitated prompt and accurate reconstruction of the bulk particle distribution by volume. Where particle size is discussed, this relates directly to the volume weighted radii recovered from laser diffraction measurements, which is akin to the mass of the particle (through density).

Central to tracking production via the PBMs is obtaining a good estimate of the PSD across all scales. This can be challenging for polydisperse cases when using LD, as larger particles can obscure smaller particles, or the optical characteristics of the nanomaterial may differ from the bulk material [31–33]. Smaller particles ($< 1$ μm) are typically under-represented using LD methods, as LD itself is volume weighted as opposed to number weighted. Further details about the process are provided in the supplementary information (SI), and in Section 2.9. To overcome this limitation, and bridge the gap between the microscale and nanoscale graphitic materials, other characterisation approaches were required to measure the contribution of the nanomaterial particles produced by the process.

### 2.4. *UV-visible-near-infrared spectroscopy*

The concentration of few-layer graphene was determined in dispersion using UV-vis-NIR spectroscopy (Perkin Elmer, Waltham Massachusetts, US, Lambda 365 UV/Vis Spectrophotometer). For this, separated supernatant samples were used. In cases where the material concentration in the supernatant was too high to measure, the supernatant was diluted at a ratio of $1 : 2$ (sample:solvent) to maintain extinction levels below ≈1 a.u. The concentration of graphene dispersions was then determined using the Lambert–Beer law and with a measured extinction coefficient of $\epsilon_{\lambda=660\text{ nm}} = 1521\text{ mg mL}^{-1}\text{ m}^{-1}$ [34]. The extinction coefficient was obtained by filtering the nanosheet dispersions through a 220 nm pore-size polytetrafluoroethylene (PTFE) membrane (Kinesis KX), oven-drying to remove the solvent, and measuring the mass of the dried product. Average layer thickness was also estimated from the extinction spectra using the empirical correlations obtained previously for liquid-exfoliated few-layer graphene by Backes

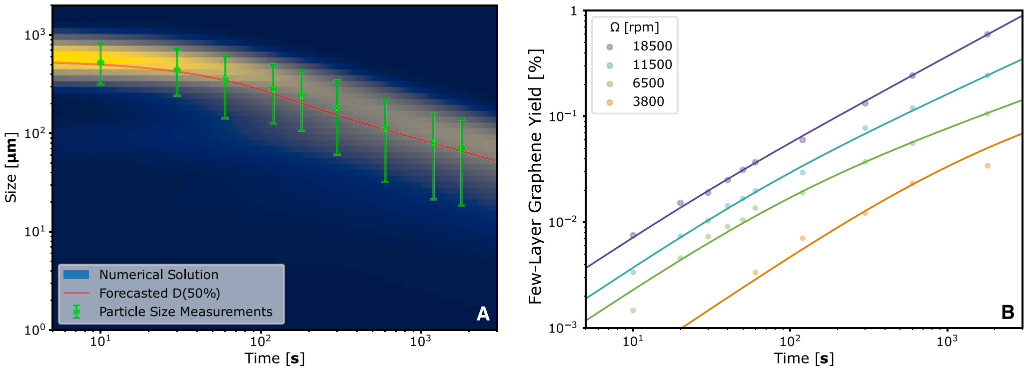

**Fig. 2.** Graphite breakup and production of few-layer graphene with exfoliation time. (A) Breakup of graphite at 11500 rpm. The PBM prediction is plotted in the background, similar to the surface illustration in Fig. 1, with colour indicating volume of material produced. Independently measured experimental PSDs are plotted as green markers denoting the 50th percentile diameter mark, with error bars stating the 10th and 90th percentile. The red line represents the numerically predicted 50th percentile. (B) Few-layer graphene yield (UV-vis-NIR concentration measurements, circular points) with fits derived from different PBMs (trendlines). The predicted concentration is from the same model defined in (A). (For interpretation of the references to colour in this figure legend, the reader is referred to the web version of this article.)

et al. [35]. Across all samples analysed, this was found to be between 4 and 7 atomic layers.

### 2.5. Nuclear magnetic resonance

Nuclear magnetic resonance (NMR) proton relaxation measurements were performed using an approach outlined for graphene dispersions [36]. NMR as a technique, magnetically perturbs the solvent molecules in solution, and then measures how long it takes for the molecules to return to equilibrium, known as the relaxation time. In solution, solvent molecules take longer to reach equilibrium than molecules adsorbed onto particles. As particle breakages produce new surface area, total surface area in solution increases, thereby leading to a reduction in relaxation time. Spin–spin (T2) relaxation measurements were performed with an Acorn Area benchtop NMR (Xigo Nanotools, Freehold New Jersey, US) operating at ∼ 13 MHz. The exact relation between the measured relaxation time $T_2$, specific surface area $\mathbf{A}$, the relaxation rate $R_{av}$ and solvent parameters is given in Eq. (1) [36].

$$\frac{1}{T_2} \equiv R_{av} = \psi \mathbf{A} K_{\mathbf{A}} + R_b \tag{1}$$

Where $\psi$ is the volume fraction, $K_{\mathbf{A}}$ is the specific surface relaxivity constant and $R_b$ is the relaxation rate of the solvent alone. To ensure representative aliquots of the system, samples were agitated for 5 mins in a light sonicating bath to break up any agglomerates, and homogeneously sampled into 1.5 mL NMR tubes. It is essential for NMR and LD measurements to maintain sample equivalency in terms of volume fraction, to avoid underrepresenting certain size fractions in solution (see SI).

### 2.6. Raman spectroscopy

Supernatant samples centrifuged at 380 RCF for 45 min were vacuum filtered through an alumina membrane with 20 nm pore size. Sufficient volume was filtered for each sample to ensure a robust coverage over the entire membrane. Raman spectroscopy was undertaken with a Renishaw inVia Qontor Raman spectroscope (Renishaw, Pontyclun UK), using a 532 nm laser employed with a 50× objective lens. A map with a 100 µm × 100 µm area (5 µm step size) was measured, for a total of 441 spectra per sample. The final averaged spectra were low pass filtered to reduce the higher frequency noise in the data.

### 2.7. Scanning electron microscopy

SEM images were taken using a Zeiss Supra scanning electron microscope by measuring secondary electrons (Carl Zeiss AG, Oberkochen, Baden-Württemberg, Germany. In lens detector, 5 kV accelerating voltage). Samples were processed at the $\Omega = 11500$ rpm impeller condition, at varying processing times (>60 s, no significant morphological differences were visible between the samples).

### 2.8. Positron emission particle tracking

Typically, particle motion within LPE systems is difficult to observe directly due to the optically opaque conditions inside the process. This imposes a challenge dealt with in previous work by limiting measurements to low material loading and early-stage periods of the process [17,29]. To complement the PBM analysis and measure the particle flow behaviour in the real exfoliation system, positron emision particle tracking (PEPT) was utilised. This approach was used to track a radioactive tracer in space with high temporal resolution (kHz). PEPT has previously been applied to evaluate a diverse range of fluid, particulate and multiphase flows [25,37,38].

As the tracer undergoes radioactive decay, it releases a pair of high energy gamma-rays in opposite directions, denoted as a singlular line of response (LoR). Taking a group of LoRs together can locate the tracer in the system [25]. To recover the positional trace from the LoRs, the Birmingham method was used [25] as implemented in the peptml library by Nicuşan and Windows-Yule [39]. In this work, two different radioactive tracers including glass beads (1 mm, quasi-spherical) and large graphite flakes (flake length between 1 to 2 mm) were considered. Graphite flakes were also the precursor materials for the graphene synthesis, providing an opportunity to directly observe the conditions inside the process (see example SI movie)). Glass beads serve as a close density match to the graphite flakes (∼ 2200 $\mathrm{kg/m^3}$), and demonstrated similar particle velocity and shear fields within the blender. As the glass beads are significantly harder than graphite flakes, it permitted study of the exfoliating conditions where graphite flakes would tend to break up very quickly, before a statistically significant number of samples could be taken.

A single particle (graphite or glass) was radioactively labelled using the University of Birmingham's cyclotron facility to produce a suitable positron-emitting radioisotope: Fluorine-18 in the case of glass and carbon-11 in the case of graphite. This tracer particle was then introduced into the LPE process and its position $(x, y, z)$ in time determined from LoRs captured using either an ADAC Forte positron camera [40] or CTI/Siemens ECAT PET scanners that were recently developed for high data rate SuperPEPT measurements [41]. Solvent, surfactant, and initial graphite concentration were maintained to match the same system conditions during graphene synthesis trials. This was also necessary given the importance of four-way particle coupling in this concentration regime (Figure S1, in the SI)

PEPT is a Lagrangian particle tracking approach. In this work, a single particle is tracked throughout the LPE process for a sufficient period of time to map out the flow behaviour across the entire batch volume (applying the assumption of an ergodic process). For visualisation purposes, and to examine particle quantities in more detail, it is useful to average these instances onto a grid; in this case, all particle quantities were averaged onto an axisymmetric grid with a $1 \times 1$ mm grid spacing. Using this grid, particle–particle shear rate was calculated following the approach of Dapelo et al. [42].

$$|\dot{\gamma}(r, y)| = \left| \frac{\partial u_r}{\partial y} + \frac{\partial u_y}{\partial r} \right| \tag{2}$$

Where $u_r$ and $u_y$ are particle velocity in the radial and axial directions of the vessel. It is important to note that the particle shear fields obtained using this method have been calculated using average graphite or glass particle velocity measurements within the blender in the radial-axial plane. Furthermore, these velocity field measurements have been obtained using one particle size at the upper end of a polydisperse distribution, and using a spatial discretisation ($1 \times 1$ mm) that is larger than most of the particles in the system. Therefore, Eq. (2) is not equivalent to the local shear rates experienced between the graphite and the solvent. Rather, it is used analogously in this work for identifying the shear distribution within the liquid exfoliation process.

Though pristine glass proved strong enough to withstand all mixer speeds, when irradiated by the cyclotron beam, particle fracture was observed randomly at all speeds, adding to the variability in the data acquired. Particle break-up, when significant, causes tracking to be lost as the LoRs become too scattered to reconstruct a trace. Irradiated glass beads would often also visibly distort in shape. Glass remained intact for longer at the higher speeds, and allowed for reconstruction of the velocity fields at speeds greater than 1500 rpm.

The flow fields and batch volumes were compared to investigate the synthesis behaviour for each LPE operating condition. By equating particle inertia to the inertial forces in the liquid, the non-dimensional speed of the particle ($u^*$) is described in Eq. (3), allowing for direct comparisons between different mixer conditions.

$$u^* = \frac{\rho_g \, u \, d_p}{\rho_l \, \omega \, d_i^2} \tag{3}$$

where $\rho_g$ is the density of the glass bead, $\rho_l$ is the density of the solvent, $\omega$ and $d_i$ are the impeller rotational speed and diameter, and $d_p$ is the particle diameter.

### *2.9. The population balance*

To model how the entire system of particles evolves with time, population balance equations (PBEs) provide a system with which to monitor the process relative to a set of input conditions. Assuming the conditions are constant in time and are self-similar to the system, there are a system of equations which model how the PSD develops. In this work, simple particle breakage (by mass fraction $f$) is defined as:

$$\frac{\partial f(v,t)}{\partial t} = \text{Birth} - \text{Death}$$

$$\frac{\partial f(v,t)}{\partial t} = \int_f^\infty k(v')\Phi(v|v') \, .df' - k(v)f(v,t) \tag{4}$$

As parent particles of volume $v'$ break, several child particles are created with volume $v$. The breakage rate $k$ is defined as a function of particle size (using the diameter of a sphere with the same volume, $x_v$) and determines the frequency with which that size is destroyed. $\Phi$ is the breakage kernel, and sets how the parent mass is distributed into the smaller mass fractions. The equation itself is a simple balance, equating the change in a particular size fraction $f$ to the fraction birthed into the size fraction minus the amount broken and distributed into different fractions. Validation of the solver and system of equations used against analytical solutions by Ziff and McGrady [43] is given in the SI. By noting the mode of breakup through empirical particle size measurements observed via LD, the form of the rate function $k$ and the kernel $\Phi$ can be determined.

$$k = \left(\frac{x_v}{B}\right)^E \tag{5}$$

$$\Phi(v|v') = l_1\left(\left(\frac{v}{v'}\right)^A\right) \tag{6}$$

Constant $A$ captures the spread of the log-normal distribution produced in this case. One further restriction within these models is that both kernels are set to be zero where $v > v'$, as no particles can break from a smaller to a larger volume. With this numerical model of the general breakup, it is possible to sum volume fractions below a cutoff, $S$, to determine the amount of small scale material produced. $S$ took a value of 1.6 μm as it provided the best fit to the experimental data across all scales and speeds measured. Indeed, this value makes practical sense, as although the nanomaterial produced through shear exfoliation are smaller by length of sheet (≈200 − 800 nm, e.g., [24,30]), the one step centrifugation process implemented here does not precisely discriminate the material, and larger particles are retained which are up to ≈2 μm [8]. Raman spectroscopy also confirmed the presence of graphitic contamination in the separated material, in Fig. 5b.

The volume based approach taken with the LD measurements is replicated here in the PBM. Fitting the PBM is performed by finding the minimum error between the LD measurements above the cutoff and the UV-vis-NIR measurements below the cutoff. For these reasons, this technique can be said to abstract detail from intermediate size ranges, as it fits to the majority of particles by volume and the region of interest.

## 3. Results and discussion

To explore breakage, impeller rotational speed was varied from below the critical exfoliation point (approximately 1500 rpm [29]) where no breakage or nanomaterial production was observed, to highly exfoliating (18500 rpm). This allowed the PBM to be fitted to a variety of conditions in the mixer. Fig. 2a demonstrates an example of the PBM fit to the LD-based PSD data for 11500 rpm, while Fig. 2b demonstrates the fit to the graphene yield measurements taken from the supernatant dispersions when summing below the cutoff $S = 1.6$ μm. This same value of $S$ was used to fit all concentration data, and was selected as it reduced error across all fits. Leaving $S$ as a constant across all speeds came at no reduction in the fit, and demonstrates that a unified model for a breakage system would only require 3 coefficients from Eq. (5) and (6) to capture the dynamics of the bulk graphitic material and nanomaterials. The other coefficients $A$, $E$ and $B$ showed a distinct trend in their value in correlation to the impeller speed (see the SI). Almost no particle breakage or production was found at the lowest speed of 1500 rpm, hence this is not included in Fig. 2.

The fit from bulk material to nanomaterial achievable through the PBM provides an argument for describing production simply as owing to breakage. While the breakage model predicts the magnitude of production well for this shear exfoliation system, it is important to highlight that in its current form, it is too simple to account for chemical effects (such as material agglomeration). Nonetheless, conceptually it is a framework that could be applied to different exfoliation processes by expanding the functions of the PBM. Note too that fitting solely to LD data alone, there is correlation but poor fit to the nanomaterial. This discrepancy means that though one could use this method to infer how production could scale from LD data, fitting from this alone omits key information. Issues fitting the PBM stem from the similar contribution between coefficients $B$, $E$ and $A$, as they all affect the prediction of

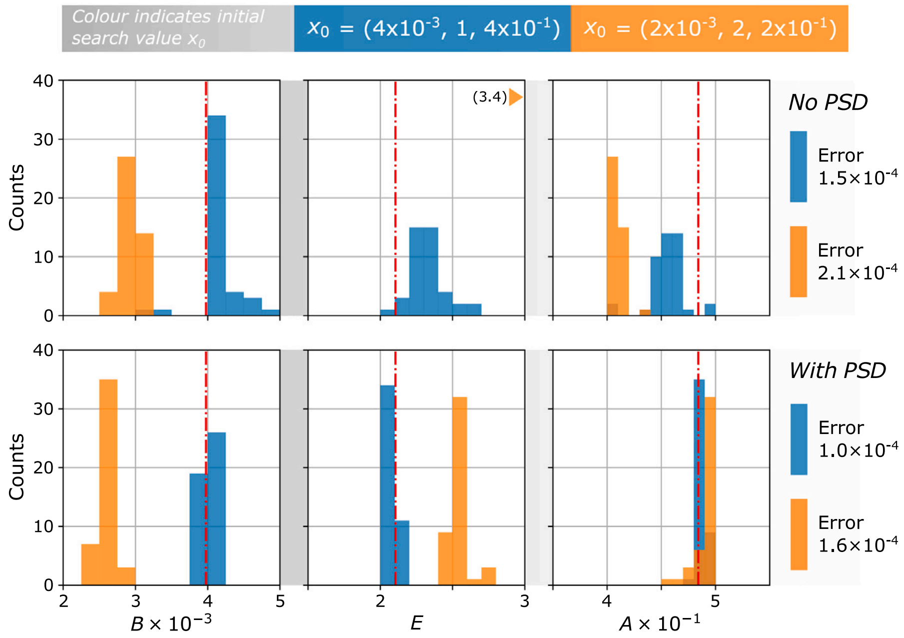

**Fig. 3.** Fitting the PBM by omitting all measurements except pairs of nanomaterial measurements, with (*With PSD*) and without (*No PSD*) inclusion of the PSD measurements as aid, for two possible coefficient starting points ($B = 4 \times 10^{-3}, E = 1, A = 4 \times 10^{-1}$ and $B = 2 \times 10^{-3}, E = 2, A = 2 \times 10^{-1}$). Histograms are constructed using the resultant coefficients, darker regions overlap. Red dashed line indicates the fully fitted solution ($4.0 \times 10^{-3}, 2.1, 4.9 \times 10^{-1}$), using all available measurements (i.e. $\Omega = 11500$ rpm condition in Fig. 2b). Final root-mean-squared error between the predicted nanomaterial trendlines are noted in the legend. (For interpretation of the references to colour in this figure legend, the reader is referred to the web version of this article.)

the smallest sizes in the distribution (i.e. the tail of the log-normal distribution). Ideally, the use of different measurement techniques that target different size ranges is essential to separate these contributions and fit the PBM. Where less breakage occurs, the PBM tends to provide a poor fit as it statistically predicts breakage occurs so long as enough time has passed. This could be because fewer particles break or that the breakage switches in mode (shattering to erosion, for example), requiring different PBM treatment [44,45].

With the suitability of this approach for predicting graphite breakup and graphene production demonstrated (Fig. 2), the effect of the number and type of sample data on the accuracy of the prediction was investigated. The similarity in effect from the coefficients in the PBM leads to an optimisation space with several local minima, and consolidates the importance of a well selected initial point ($x_0$) to avoid perturbing the PBM during fitting. For this initial condition, PSD measurements provide an excellent technique to establish an estimate for the coefficient value ($B$, $E$, $A$ and $S$ depending on method of separation)[1]. Once an initial value for these coefficients is known, it is simple to solve for the PBM with a small number of few-layer material yield measurements. To study the stability of the solution, various PBM coefficients were selected based on their best fit to a reduced selection of data under the $\Omega = 11500$ rpm impeller condition in Fig. 2. Presented in Fig. 3, all possible combinations of two points from the selection of few-layer yield measurements (Fig. 2b, $\Omega = 11500$ rpm) were selected and fitted with or without the addition of LD PSD measurements (Fig. 2a). This test was repeated with two pre-established initial values ($x_0$), based on the PSD solution ($B = 4 \times 10^{-3}, E = 1, A = 4 \times 10^{-1}$; $B = 2 \times 10^{-3}, E = 2, A = 2 \times 10^{-1}$). One of these points ($4 \times 10^{-3}, 1, 4 \times 10^{-1}$) is expected to perform better, as the relative difference in the initial value is similar to that in the final result. The histograms show remarkable coherence towards specific minima and vary little in spite of the lack of information used to construct them, but they also show that a poor initial value can lead to inaccurate results, a pitfall often encountered in optimisation related problems such as this. If the rough order of magnitude for the coefficients is known for the specific exfoliating condition, it is possible to fit the PBM with relatively few measurements. To summarise, PSD measurements across all scales are essential to obtain a good starting point for the PBM and to understand the mode of breakage. Nanomaterial measurements are essential for tracking production, but relatively few of these nanomaterial measurements are needed to enable an accurate estimation of the coefficients. Here, root-mean-squared errors of 0.01–0.016% are introduced when using only two concentration measurements with PSD measurements to construct the PBM for this impeller speed. This is a significant advantage, given the extensive time required to sample, post-process, and characterise nanomaterials from liquid exfoliation processes.

To assess the validity of the breakage model under different initial distributions, a representative quantity of larger graphitic material was sifted from the store of flake graphite and exposed to the 11500 rpm impeller speed ("Large particles", red PSD in Fig. 4). The tests ran with larger graphite particles were compared to tests using unsifted material ("Small particles", green PSD) at the same impeller condition. The experiments initialised with the larger material ran at a lower concentration 4 mg/mL, enough so as to not alter the conditions inside the blender, but still capture their effect with limited material. A comparison of the PBM's performance to acquired LD PSD data is presented in Fig. 4. In both cases, the distributions differ initially and coalesce to become near identical within the first minute of processing. It shows that for a specific exfoliating condition, assuming particle material properties are maintained when scaled, a single model can capture the underlying dynamics as a function of the particle size. This independence between the conditions in the vessel and particle size demonstrates that a PBM is robust for analysing and predicting these types of mechanochemical synthesis processes.

An interesting implication of Eq. (6), is that for a parent particle size of unity, the shape of the kernel is defined by Eq. (7):

$$P(v) = A\left(\frac{1}{v}\right)^{1-A}\Bigg|_{v<1} \tag{7}$$

---

[1] Rough coefficient bounds can be manually estimated by examining where the solution is stable.

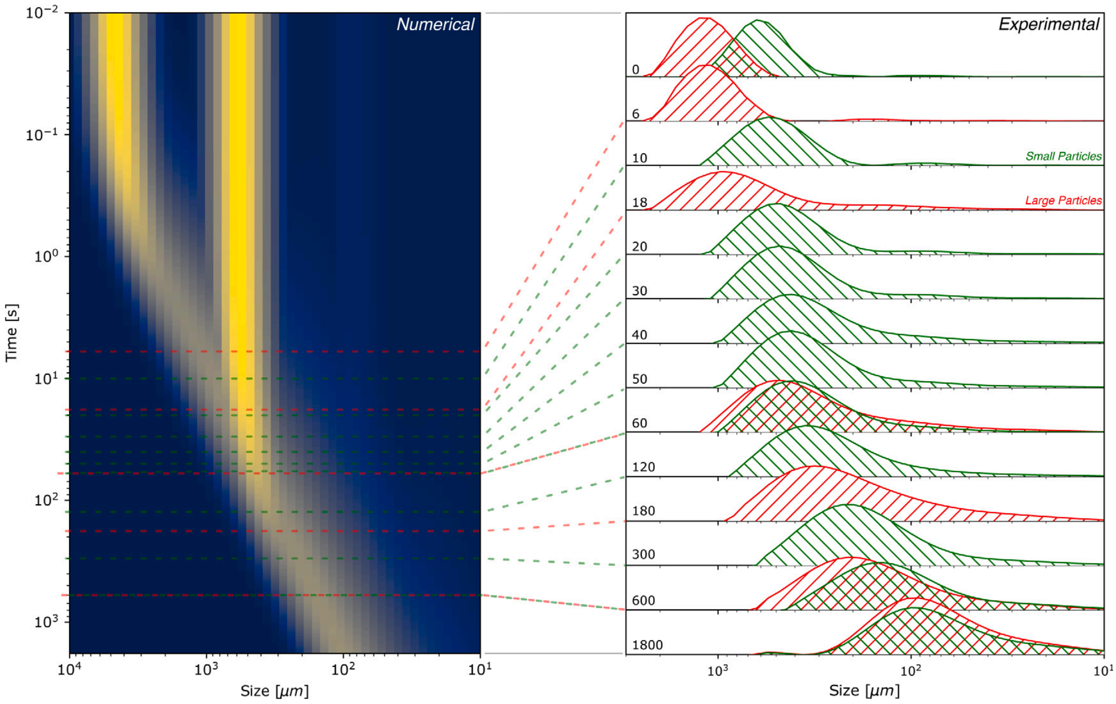

**Fig. 4.** Graphite breakup for two different starting size distributions. Left, both PSDs are plotted on a continuous colour plot (colour indicating volume of material produced) breaking under the influence of the same fractional PBM in time. Red and Green dashed lines mark the times at which experimental LD samples were taken. Right, two different starting distributions are exposed to the same exfoliation conditions (surfactant concentration of 4.3 mg/mL and impeller speed of 11500 rpm; but different starting concentrations of 4 mg/mL for the larger particles, and 20 mg/mL for the smaller particles). (For interpretation of the references to colour in this figure legend, the reader is referred to the web version of this article.)

As $v$ approaches 0, $P(v)$ increases with $1/v$, effectively showing that this method of breakage has a high probability to break into small $v$, indicative of an attritive process [45]. When $A = 1$ there is equivalent breakage into all sizes, i.e. random breakage. The kernel function is process specific, and though a power-law fit certainly describes the process happening herein, it depends entirely on how the parent material is broken. This suggests that the PBM approach applies more broadly to other methods of LPE, and that similar exfoliating techniques promote efficient production of 2DMs as the breakage kernel is skewed towards smaller sizes.

Measurements of Raman spectra normalised to the G-peak in Fig. 5 uncovered changes in the product structure as liquid exfoliation proceeded. Raman spectral peaks, labelled G, D, D' and 2D, evolve in time to reveal the material conversion from bulk graphitic behaviour into few-layer graphene. The shape of the 2D peak from the stepped shape typical of bulk graphite at 10 s changed to resemble that of fewer layer graphite (2–5 atomic layers) by 180 s [46]. Fig. 5 also shows a presence and subsequent growth in the D ( $1350\ \mathrm{cm}^{-1}$) and D' ( $1620\ \mathrm{cm}^{-1}$) bands, settling on a distinctive shape beyond 180 s. The growth of the D and D' bands are associated with an increase in nanomaterial defects. For shear exfoliation processes on this precursor material, these are known to be due to nanosheet edges rather than basal plane defects, suggesting that the separated material is becoming smaller and therefore has more edges [8,30].

The histograms in Fig. 5a confirm that for early synthesis times ($0 - 120$ s) the $I_D/I_G$ ratio is skewed towards bulk graphite characteristics ($I_D/I_G \approx 0.2$). The measurement statistics for $>$ 180 s illustrate a shift in the mode with more of the product displaying characteristics of few-layer graphene ($I_D/I_G \approx 0.5$). This trend with process time is in agreement with the PBM predictions which show a significant broadening of the PSD tail into smaller size fractions when the exfoliation time exceeds ≈120 s (Fig. 4). The progression of Raman spectra in Fig. 5b show the presence of graphite especially in samples taken early in the exfoliation run, suggesting that the one-step method of separation implemented here does not exactly discriminate the few-layered material.

Another benefit of PBMs is the ability for them to be used as a tool for predicting potential future production (up to $t \rightarrow \infty$) assuming that production is not limited by extraneous factors (see Fig. 6). Some limiting examples that have been observed are:

- Solubility, saturation and reaggregation. An example of system saturation was shown by Stafford et al. [17] using Taylor–Couette exfoliation.
- A drop in the breakage rate past a certain size, which has been shown to be the case in studies with carbon nanotubes and graphene [47].
- Increasing nanomaterial concentration over time will result in changes to the apparent liquid mixture properties, including viscosity and density which would have an effect on production.

Though not an exhaustive list, these factors would be challenging to correct for unless enough accurate preliminary measurements had been taken across a range of scales. With current LD techniques this could prove difficult to measure depending on the material [32], as discussed earlier in Section 2.

The production curves given in Fig. 6a are provided to demonstrate two aspects of the current breakage model. Firstly, that when yield in LPE is unrestricted by other factors, it takes on a piece-wise power-law form. This starts with a region of highest production, where large bulk particles break superlinearly to form a log-normal distribution; followed by breakup towards the smaller sizes with rate $E$. Secondly, the model further conserves mass by default, reaching 100%wt yield by the end of the run. The extrapolation in Fig. 6a shows the time taken to reach 90%wt yield between the top two speeds differs on the order of months. Of course, these extreme scenarios are not practical, however, it illustrates that through the use of the PBM approach, it would be possible to explore and optimise system-level process efficiencies and trade-offs (e.g., energy consumption, yield, production rate, operating

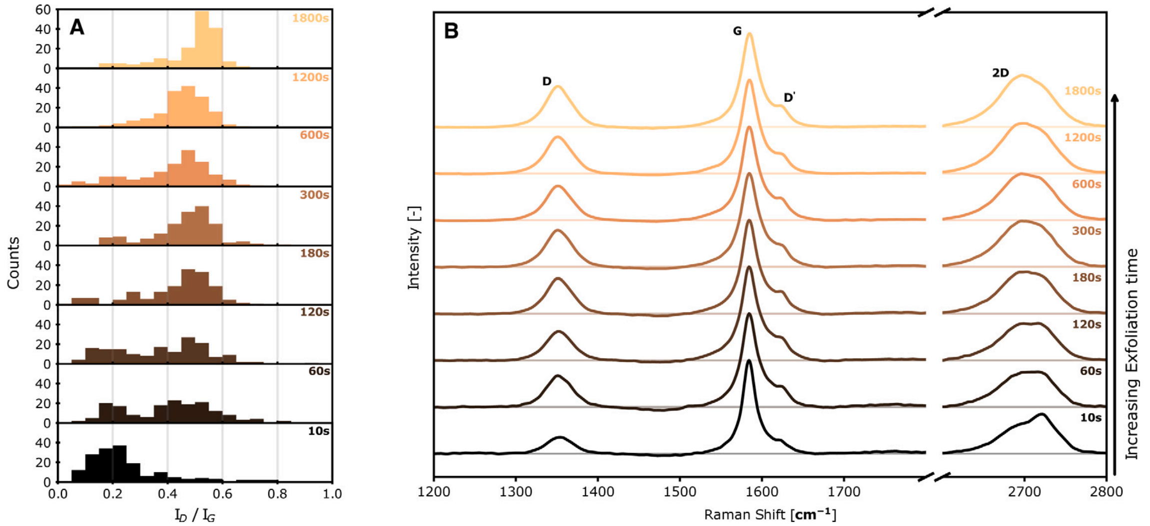

**Fig. 5.** Evolution of the spectroscopic characteristics of separated few-layer graphene samples with process time. (A) Statistical distributions of peak intensities $I_D/I_G$. (B) Averaged Raman spectra normalised to the G peak. Measurements correspond to $\Omega = 11500$ rpm impeller condition.

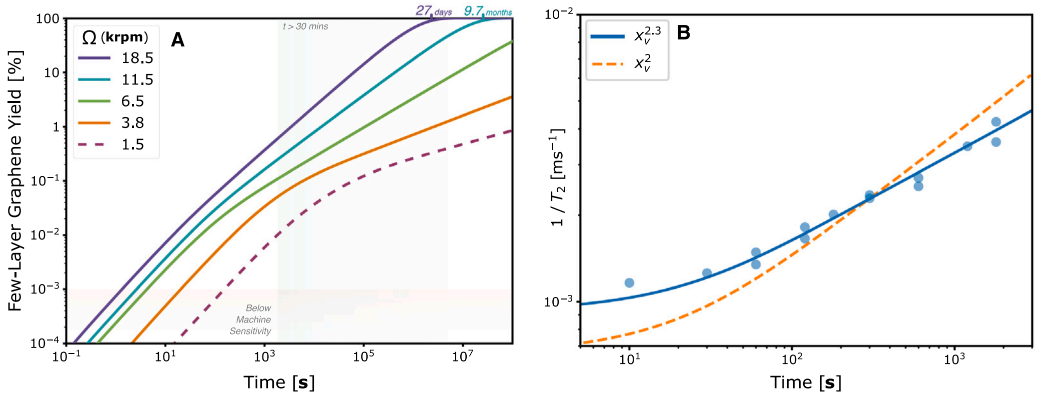

**Fig. 6.** Forecasting graphene production yields and particle surface area using the PBM, assuming no change significant change in breakage mode. (a) The PBM is extrapolated to $t \rightarrow \infty$ to view the extents of production. The lowest speed was fitted only to the LD measurement even though there was very little to no breakup, as there was no measurable increase in nanomaterial concentration (represented as a dashed line). (b) NMR measurements are compared to the PBM predicted surface area ($\Omega = 11500$ rpm). Two predictions are used, based on $x_v$ (volume based diameter), spherical surface area $\approx x_v^2$ and accounting for the rough surface area $\approx x_v^{2.3}$.

costs). Furthermore, there are a variety of graphitic nanomaterials that have different applications based on their size. This includes graphite flakes with thicknesses of up to 200 nm [15], and few-layer material with thicknesses typically below 3 nm. The PBM approach described in this study could also be used to predict the fractions (and yields) of these different synthesis products, representing an important step away from linear regression, and towards physically constrained and informed models.

In conjunction with NMR measurements, the PBM can be used as a predictor of the rate of surface area increase in the product. Examining Eq. (1), if $\psi$, $K_{\mathbf{A}}$ and $R_b$ remain constant, surface area represents the only parameter changing in Fig. 6b. Comparing to the PBM, it is evident that simply using the (minimum) spherical surface area obtained with the diameter estimated from the volume of the particle ($x_v$) was not enough to provide an accurate fit, though suitable approximations can be made for a better fit. As graphite particles typically exhibit some surface roughness at all scales caused by inter-grain boundaries, a level of self-similarity between particles is visible, with very little change in the particle shape observed from optical measurements (see hydro-insight imaging in the SI). In this case, as the shape does not change drastically between the large and small size fractions, the surface area should scale with $x_v^D$, where $D$ is limited between $2 < D < 3$, with the lower limit indicating a perfectly smooth surface and the higher limit a surface which completely fills all available space. A value of $D = 2.3$ was found to closely fit the NMR measurements and agrees with empirical measurements taken by Persson [48], who found that most brittle fractures typically cause self-affine surfaces with $D \approx 2.2$.

The dynamics behind the graphite breakup process were investigated by obtaining particle velocity measurements *in operando* for the liquid exfoliation process. Fig. 7 shows the particle flow behaviour within the vessel spanning a range of impeller speeds from $\Omega = 1500$ rpm to 11500 rpm. Here, a glass bead (density-matched with graphite) was tracked within the batch to map out the flow behaviour. This was necessary to overcome particle tracking challenges associated with graphite tracer breakup at speeds > 1500 rpm (see the SI).

A comparison of the flow regimes between graphite and glass at the lowest speed (1500 rpm) can be seen in Fig. 8. Though both sets of particles behaved similarly in speed and particle–particle shear (the latter is pictured in Figs. 8a-b), the residency maps in the SI show the glass tracers tended to reside away from the bulk flow regions of interest. Though graphite also demonstrated an affinity to the same regions as the glass bead, it spent much more time in the fluid as a whole.

Using the particle velocity fields in Fig. 7, it is possible to capture the intra-particle shear rate, shown in Fig. 8. This particle–particle shear rate aligned well with theoretical scaling estimates (Phipps [49],

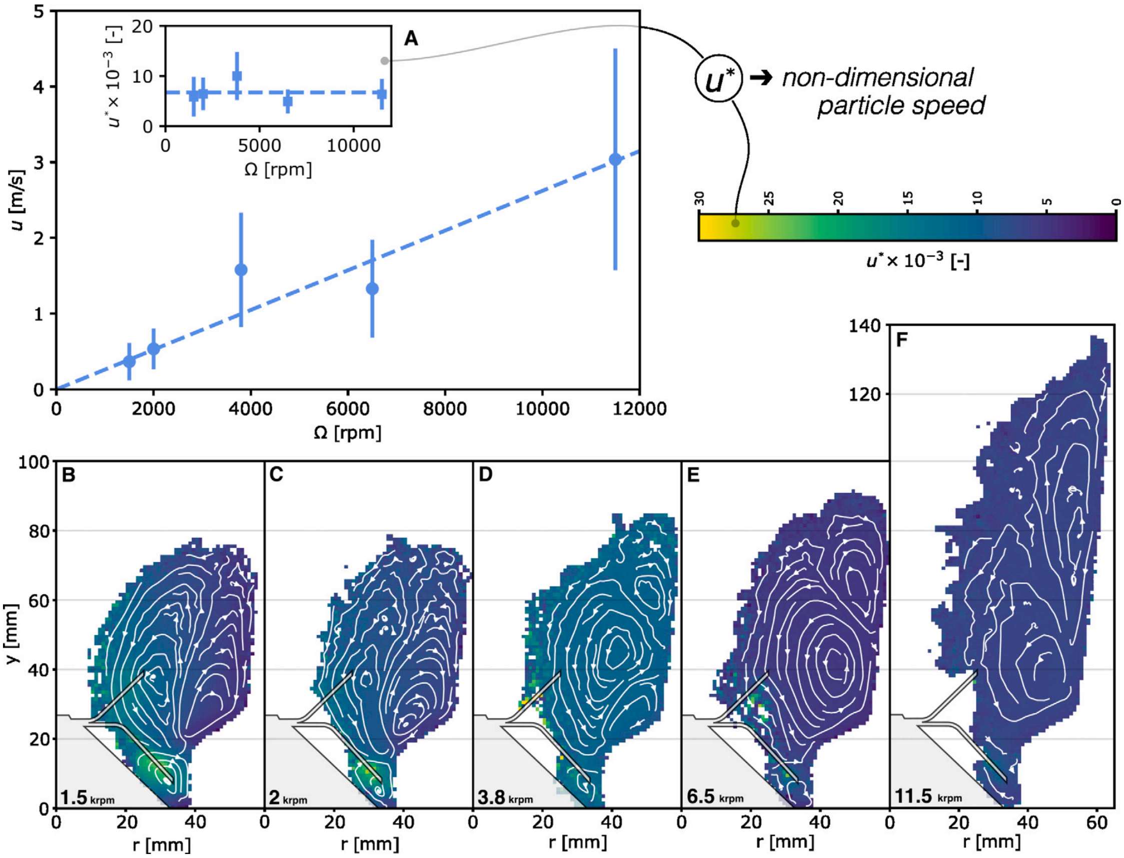

**Fig. 7.** Particle velocity within the kitchen blender using a glass bead tracer. (A) Mean particle velocity with impeller speed. Error bars indicate one standard deviation in particle velocity, and inset figure shows the non-dimensionalised particle speed, $u^*$, from Eq. (3). (B-F) Reconstructed flow fields while operating at differing impeller speeds (with impeller geometry overlay), depicting a cross-section of the blender in operation.

Fig. 8c) for the actual shear rate in similar stirred batch reactors, as both the 90th percentile and the 50th percentile (by axisymmetric area) produced a scaling with respect to impeller speed $\Omega$ of $\dot{\gamma} \sim \Omega^{1.5}$ [49]. Fig. 8d presents isobars of particle–particle shear rate, with a green line to indicate the impeller speed at which few-layer graphene production was first observed ($\Omega = 3800$ rpm). Paton et al. [8] found the shear rate of production to be around $\dot{\gamma}_{\mathrm{crit}} \approx 1 \times 10^4\ \mathrm{s}^{-1}$ for graphene. For reasons outlined in Section 2.8, the particle–particle shear rate measurements in this work are only representative of the shear field distribution within the exfoliation system, and never exceed $\dot{\gamma} \sim 10^4\ \mathrm{s}^{-1}$ across all speeds measured. Residence itself is given as a percentage of the total time spent in the dispersion. It is important to note that residency seemed to differ significantly between glass and graphite tracers, due largely to how the glass bead seemed to spend less time within the bulk fluid regions. For the speeds measured, a residency comparison between the two tracers is given in the SI. Despite the necessary compromises with tracer particle selection, the trends in Fig. 8 demonstrate that with increasing impeller speed, precursors will experience both an increase in shear rate and exposure time to these higher levels of shear. This facilitates the increased frequency and likelihood of particle breakup events, resulting in significant differences in the concentration of few-layer graphene (Fig. 2) and production times forecast for different impeller speeds (Fig. 6).

Interestingly, the glass particle flow fields (Fig. 7) demonstrate shifts in the circulation patterns within the mixer. Initially separated into three distinct circulations, the central circulation eventually dominates as speed increases, and moves away from the path of the blades. As the immediate region surrounding the blades (i.e. $r < 34$ mm, $y < 40$ mm, see S11 in the SI) is associated with blade impacts and high shear, reduced residency here should correspond to a reduced efficacy in production. To examine the change in the volume swept by the blades, the mixer was analysed as two separate compartments, in the style of Alves et al. [50]. The first compartment contains the blades ($r < 34$ mm, $y < 40$ mm) and is associated with particle-blade interactions, while the remaining vessel comprises the second compartment, representing the majority of the time spent by the particle in the vessel. Comparing the time the particle spent resident inside the first compartment as opposed to the mixer as a whole represents a close analog to ‘residence time’, $t_r$, discussed in other works [17,29]. This $t_r$ is found to scale inversely with the impeller speed, $t_r \sim \Omega^{-0.65}$. Using spinning disk and Taylor–Couette reactors, Stafford et al. [17] ascribes few-layer graphene concentration ($C_g$) to scale with $C_g \sim \dot{\gamma} t_r$. This was also found to agree with the characteristic timescale predicted for complete sliding of bi-layer sheets under shear flow [11]. Combining this with our measurements for shear rate scaling in this work ($\dot{\gamma} \sim \Omega^{1.5}$, also in agreement with theoretical scaling [49], Fig. 8c), arrives at a few-layer graphene concentration scaling of $C_g \sim \Omega^{0.85}$. This solution correlates to the few-layer concentration measurements, which ascribe a scaling closer to linear ($C_g \sim \Omega$). See the SI for more detail on this analysis. Our work therefore confirms that the underlining mechanisms behind shear exfoliation processes have similarity, despite the wide diversity of production approaches that are available. Similarly, this supports the idea that the PBM approach presented can have general applicability for predicting nanosheet synthesis via liquid phase exfoliation.

## 4. Conclusion

In this paper, a method for modelling the production of few-layer graphene within liquid exfoliation processes was developed and validated following a population balance approach. For high-shear, turbulent, impeller-driven blending systems, the breakup process was found

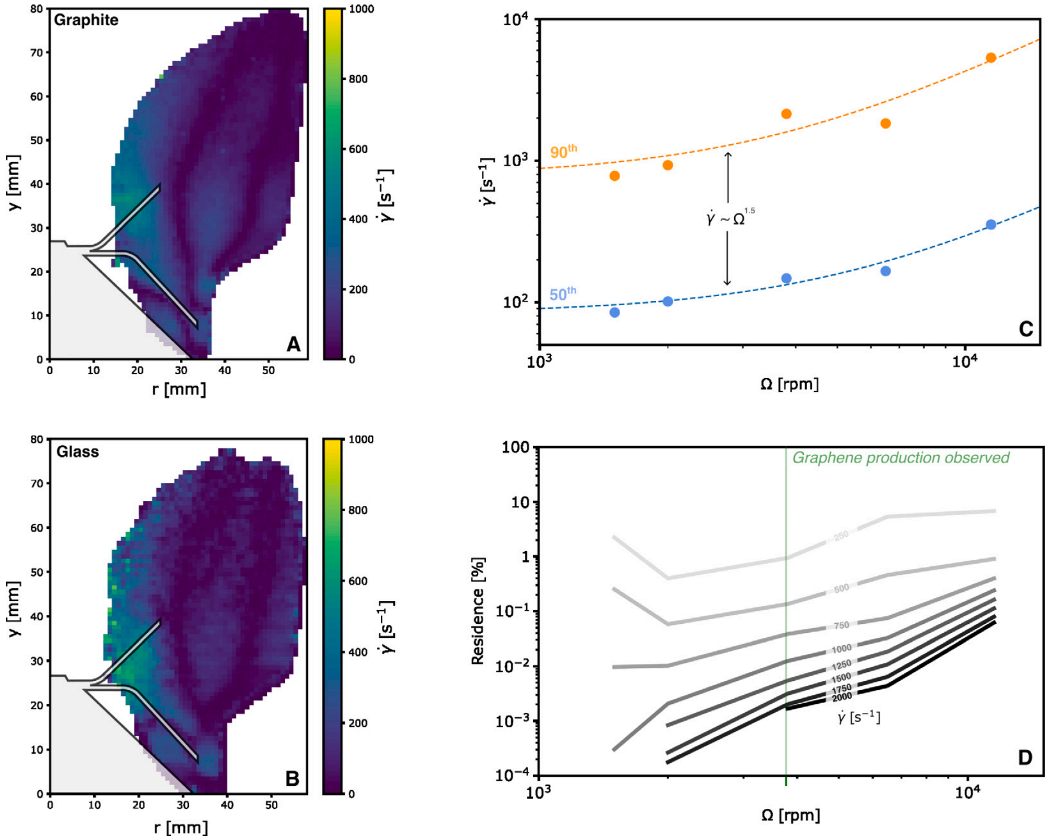

**Fig. 8.** Graphite particle hydrodynamics within the liquid exfoliation system. Particle–particle shear rate fields at the lowest rotor speed (1500 rpm) for (A) graphite and (B) glass. (C) Scaling of the 90th and 50th percentile particle–particle shear rate with impeller speed. (D) The percentage of time a particle spends under the influence of different minimum shear rates. Dashed line represents the point at which nanomaterial production is first observed.

to obey simple breakage kernel and rate functions that were determined from observations of graphitic particle size distributions. A complete description of the exfoliation process was possible by implementing only three coefficients within this model, which were found to be sensitive to impeller rotational speed. The robustness was shown by the ability to correctly predict the evolution of graphitic particle size distributions that originated from different starting precursor sizes. By modelling the evolution of the full particle size distribution, the approach captures various carbon materials that have practical use in many applications, including few-layer graphene and GNP. Examination of the breakage model revealed physical insights on the breakage mechanisms. The high shear process used in this work produces a high probability for large particle breakup into small particles, indicative of an attritive process. This was confirmed with statistical Raman spectroscopy measurements which revealed a rapid conversion from graphitic to few-layer graphene materials in the first minutes of the process. We show that when coupled with nuclear magnetic resonance spectroscopy measurements performed on dispersions of graphitic materials, the model can also integrate particle surface area characteristics. The dynamics within the graphene synthesis system were explored by performing positron emission particle tracking to determine the graphite particle velocity, shear rate and residence distributions. This showed that increasing impeller speed leads to a combined positive effect, increasing shear rate and the residence time of particles in areas of high shear in the system. This leads to the higher probability of breakup that was observed by the population balance models and graphene concentration data for increasing speeds. As the population balance requires empirical data to construct, an assessment on reduced sampling showed that the PSD data was important to use as an input, yet only a limited set of few-layer graphene concentration measurements were necessary to reconstruct the original model within 0.02%. Importantly, the population balance method is agnostic to the measurement technique used to determine the particle size distribution and graphene concentrations, which allows for the approach to be extended to other materials characterisation data available (e.g., statistical AFM, TEM). Moreover, the population balance method is well developed for the analysis of systems of breakage and agglomeration, suggesting it can be extended to other two-dimensional materials that are produced using similar mechanochemical approaches (e.g., Transition Metal Dichalcogenides). Overall, this provides a promising avenue for creating physics-based predictive models of top-down synthesis, opening up opportunities to forecast long-duration product yields from shorter duration tests, and design synthesis approaches that improve process intensification, optimisation, and material sustainability.

## CRediT authorship contribution statement

**Diego T. Perez-Alvarez:** Writing – original draft, Visualization, Validation, Software, Methodology, Investigation, Formal analysis, Conceptualization. **Sofia Marchesini:** Writing – review & editing, Supervision, Methodology, Investigation, Formal analysis, Conceptualization. **Keith R. Paton:** Writing – review & editing, Supervision, Methodology, Investigation, Formal analysis. **Jack Sykes:** Writing – review & editing, Formal analysis. **Dawid Hampel:** Writing – review & editing, Investigation. **Jennifer Burt:** Writing – review & editing, Methodology, Investigation, Formal analysis. **Konstantinos Despotelis:** Methodology, Investigation. **Diogo Fernandes:** Supervision, Methodology. **Philip Davies:** Writing – review & editing, Supervision. **Christopher Windows-Yule:** Writing – review & editing, Supervision, Methodology. **Tzany Kokalova Wheldon:** Writing – review & editing, Supervision, Resources, Methodology. **Andrew J. Pollard:** Writing – review & editing, Supervision, Resources, Methodology. **Jason Stafford:** Writing – review & editing, Supervision, Methodology, Funding acquisition, Conceptualization.

## Declaration of competing interest

The authors declare that they have no known competing financial interests or personal relationships that could have appeared to influence the work reported in this paper.

## Acknowledgements

This work was supported by the EPSRC DTP, United Kingdom [EP/T517926/1] and a Royal Academy of Engineering/Leverhulme Trust Research Fellowship, United Kingdom [LTRF2122-18-108]. SM, KRP, KD and AJP would like to acknowledge the National Measurement System (NMS) of the Department for Science, Innovation and Technology (DSIT), United Kingdom, UK (projects #127931 and #128807, Enabling innovation to meet UK Net Zero targets through physicochemical metrology of nanoscale advanced materials, United Kingdom) for funding. The authors would also like to acknowledge William Lee and Caterina Minelli for reviewing the manuscript.

## Appendix A. Supplementary data

Supplementary material related to this article can be found online at https://doi.org/10.1016/j.carbon.2024.119687.

## References

[1] K.S. Novoselov, A.K. Geim, S.V. Morozov, D. Jiang, Y. Zhang, S.V. Dubonos, I.V. Grigorieva, A.A. Firsov, Electric field effect in atomically thin carbon films, Science 306 (5696) (2004) 666–669, http://dx.doi.org/10.1126/science.1102896.

[2] E. Shamsaei, F.B. Souza, X. Yao, E. Benhelal, A. Akbari, W. Duan, Graphene-based nanosheets for stronger and more durable concrete: A review, Constr. Build. Mater. 183 (2018) 642–660, http://dx.doi.org/10.1016/j.conbuildmat.2018.06.201.

[3] D.T. Pérez-Álvarez, J. Brown, E.A. Elgohary, Y.M.A. Mohamed, H.A. El Nazer, P. Davies, J. Stafford, Challenges surrounding nanosheets and their application to solar-driven photocatalytic water treatment, Mater. Adv. 3 (10) (2022) 4103–4131, http://dx.doi.org/10.1039/D2MA00276K.

[4] M. Tawalbeh, H.A. Khan, A. Al-Othman, Insights on the applications of metal oxide nanosheets in energy storage systems, J. Energy Storage 60 (2023) 106656, http://dx.doi.org/10.1016/j.est.2023.106656.

[5] Z. Wang, X. Yan, Q. Hou, Y. Liu, X. Zeng, Y. Kang, W. Zhao, X. Li, S. Yuan, R. Qiu, M.H. Uddin, R. Wang, Y. Xia, M. Jian, Y. Kang, L. Gao, S. Liang, J.Z. Liu, H. Wang, X. Zhang, Scalable high yield exfoliation for monolayer nanosheets, Nature Commun. 14 (236) (2023) 1–8, http://dx.doi.org/10.1038/s41467-022-35569-8.

[6] S.N. Alam, N. Sharma, L. Kumar, Synthesis of graphene oxide (go) by modified hummers method and its thermal reduction to obtain reduced graphene oxide (rgo), Graphene 6 (1) (2017) 1–18.

[7] T.C. Achee, W. Sun, J.T. Hope, S.G. Quitzau, C.B. Sweeney, S.A. Shah, T. Habib, M.J. Green, High-yield scalable graphene nanosheet production from compressed graphite using electrochemical exfoliation, Sci. Rep. 8 (14525) (2018) 1–8, http://dx.doi.org/10.1038/s41598-018-32741-3.

[8] K.R. Paton, E. Varrla, C. Backes, R.J. Smith, U. Khan, A. O'Neill, C. Boland, M. Lotya, O.M. Istrate, P. King, T. Higgins, S. Barwich, P. May, P. Puczkarski, I. Ahmed, M. Moebius, H. Pettersson, E. Long, J. Coelho, S.E. O'Brien, E.K. McGuire, B.M. Sanchez, G.S. Duesberg, N. McEvoy, T.J. Pennycook, C. Downing, A. Crossley, V. Nicolosi, J.N. Coleman, Scalable production of large quantities of defect-free few-layer graphene by shear exfoliation in liquids, Nature Mater. 13 (2014) 624–630, http://dx.doi.org/10.1038/nmat3944.

[9] K. Clifford, S.P. Ogilvie, A. Amorim Graf, H.J. Wood, A.C. Sehnal, J.P. Salvage, P.J. Lynch, M.J. Large, A.B. Dalton, Emergent high conductivity in size-selected graphene networks, Carbon 218 (2024) 118642, http://dx.doi.org/10.1016/j.carbon.2023.118642.

[10] J. Brown, J. Stafford, Exploring feedstock recycling in liquid-phase-exfoliated nanosheets, ACS Sustain. Chem. Eng. 12 (39) (2024) 14363–14370, http://dx.doi.org/10.1021/acssuschemeng.4c05845.

[11] G. Salussolia, C. Kamal, J. Stafford, N. Pugno, L. Botto, Simulation of interacting elastic sheets in shear flow: Insights into buckling, sliding, and reassembly of graphene nanosheets in sheared liquids, Phys. Fluids 34 (5) (2022) 053311, http://dx.doi.org/10.1063/5.0087192.

[12] K.R. Paton, J. Anderson, A.J. Pollard, T. Sainsbury, Production of few-layer graphene by microfluidization, Mater. Res. Express 4 (2) (2017) 025604, http://dx.doi.org/10.1088/2053-1591/aa5b24.

[13] Y. Arao, M. Kubouchi, High-rate production of few-layer graphene by high-power probe sonication, Carbon 95 (2015) 802–808, http://dx.doi.org/10.1016/j.carbon.2015.08.108.

[14] Y. Hernandez, V. Nicolosi, M. Lotya, F.M. Blighe, Z. Sun, S. De, I.T. McGovern, B. Holland, M. Byrne, Y.K. Gun'Ko, J.J. Boland, P. Niraj, G. Duesberg, S. Krishnamurthy, R. Goodhue, J. Hutchison, V. Scardaci, A.C. Ferrari, J.N. Coleman, High-yield production of graphene by liquid-phase exfoliation of graphite, Nature Nanotechnol. 3 (9) (2008) 563–568, http://dx.doi.org/10.1038/nnano.2008.215.

[15] P.G. Karagiannidis, S.A. Hodge, L. Lombardi, F. Tomarchio, N. Decorde, S. Milana, I. Goykhman, Y. Su, S.V. Mesite, D.N. Johnstone, R.K. Leary, P.A. Midgley, N.M. Pugno, F. Torrisi, A.C. Ferrari, Microfluidization of graphite and formulation of graphene-based conductive inks, ACS Nano 11 (3) (2017) 2742–2755, http://dx.doi.org/10.1021/acsnano.6b07735.

[16] Y. Arao, Y. Mizuno, K. Araki, M. Kubouchi, Mass production of high-aspect-ratio few-layer-graphene by high-speed laminar flow, Carbon 102 (2016) 330–338, http://dx.doi.org/10.1016/j.carbon.2016.02.046.

[17] J. Stafford, N. Uzo, U. Farooq, S. Favero, S. Wang, H.-H. Chen, A. L'Hermitte, C. Petit, O.K. Matar, Real-time monitoring and hydrodynamic scaling of shear exfoliated graphene, 2D Mater. 8 (2) (2021) 025029, http://dx.doi.org/10.1088/2053-1583/abdf2f.

[18] L. Botto, Toward nanomechanical models of liquid-phase exfoliation of layered 2D nanomaterials: Analysis of a $\pi$ - peel model, Front. Mater. 6 (2019) 448137, http://dx.doi.org/10.3389/fmats.2019.00302.

[19] G. Salussolia, E. Barbieri, N.M. Pugno, L. Botto, Micromechanics of liquid-phase exfoliation of a layered 2D material: A hydrodynamic peeling model, J. Mech. Phys. Solids 134 (2020) 103764, http://dx.doi.org/10.1016/j.jmps.2019.103764.

[20] Y. Hernandez, M. Lotya, D. Rickard, S.D. Bergin, J.N. Coleman, Measurement of multicomponent solubility parameters for graphene facilitates solvent discovery, Langmuir 26 (5) (2010) 3208–3213, http://dx.doi.org/10.1021/la903188a.

[21] A. Griffin, K. Nisi, J. Pepper, A. Harvey, B.M. Szydłowska, J.N. Coleman, C. Backes, Effect of surfactant choice and concentration on the dimensions and yield of liquid-phase-exfoliated nanosheets, Chem. Mater. 32 (7) (2020) 2852–2862, http://dx.doi.org/10.1021/acs.chemmater.9b04684.

[22] A. Liscio, K. Kouroupis-Agalou, X.D. Betriu, A. Kovtun, E. Treossi, N.M. Pugno, G.D. Luca, L. Giorgini, V. Palermo, Evolution of the size and shape of 2d nanosheets during ultrasonic fragmentation, 2D Mater. 4 (2) (2017) 025017, http://dx.doi.org/10.1088/2053-1583/aa57ff.

[23] Z. Li, R.J. Young, C. Backes, W. Zhao, X. Zhang, A.A. Zhukov, E. Tillotson, A.P. Conlan, F. Ding, S.J. Haigh, K.S. Novoselov, J.N. Coleman, Mechanisms of liquid-phase exfoliation for the production of graphene, ACS Nano 14 (9) (2020) 10976–10985, http://dx.doi.org/10.1021/acsnano.0c03916.

[24] D.T. Pérez-Álvarez, J. Brown, J. Stafford, Modification of kitchen blenders into controllable laboratory mixers for mechanochemical synthesis of atomically thin materials, HardwareX 16 (2023) 00471, http://dx.doi.org/10.1016/j.ohx.2023.e00471.

[25] D.J. Parker, C.J. Broadbent, P. Fowles, M.R. Hawkesworth, P. McNeil, Positron emission particle tracking - a technique for studying flow within engineering equipment, Nucl. Instrum. Methods Phys. Res. A 326 (3) (1993) 592–607, http://dx.doi.org/10.1016/0168-9002(93)90864-E.

[26] I. Chen, S. Cassaro, Physiology, Bile Acids, National Library of Medicine, 2023, https://www.ncbi.nlm.nih.gov/books/NBK549765.

[27] T. Ivanković, J. Hrenović, Surfactants in the environment, Arch. Ind. Hygiene Toxicol. 61 (1) (2010) 95–110, http://dx.doi.org/10.2478/10004-1254-61-2010-1943.

[28] S. Elghobashi, On predicting particle-laden turbulent flows, Appl. Sci. Res. 52 (4) (1994) 309–329, http://dx.doi.org/10.1007/BF00936835.

[29] D.T. Pérez-Álvarez, P. Davies, J. Stafford, Foam flows in turbulent liquid exfoliation of layered materials and implications for graphene production and inline characterisation, Chem. Eng. Res. Des. 177 (2022) 245–254, http://dx.doi.org/10.1016/j.cherd.2021.10.041.

[30] E. Varrla, K.R. Paton, C. Backes, A. Harvey, R.J. Smith, J. McCauley, J.N. Coleman, Turbulence-assisted shear exfoliation of graphene using household detergent and a kitchen blender, Nanoscale 6 (20) (2014) 11810–11819, http://dx.doi.org/10.1039/C4NR03560G.

[31] J. Amaro-Gahete, A. Benítez, R. Otero, D. Esquivel, C. Jiménez-Sanchidrián, J. Morales, Á. Caballero, F.J. Romero-Salguero, A comparative study of particle size distribution of graphene nanosheets synthesized by an ultrasound-assisted method, Nanomaterials 9 (2) (2019) http://dx.doi.org/10.3390/nano9020152.

[32] M.K. Rabchinskii, S.D. Saveliev, S.A. Ryzhkov, E.K. Nepomnyashchaya, S.I. Pavlov, M.V. Baidakova, P.N. Brunkov, Establishing the applicability of the laser diffraction technique for the graphene oxide platelets lateral size measurements, J. Phys. Conf. Ser. 1695 (1) (2020) 012070, http://dx.doi.org/10.1088/1742-6596/1695/1/012070.

[33] V. Filipe, A. Hawe, W. Jiskoot, Critical evaluation of nanoparticle tracking analysis (NTA) by NanoSight for the measurement of nanoparticles and protein aggregates, Pharm. Res. 27 (5) (2010) 796–810, http://dx.doi.org/10.1007/s11095-010-0073-2.

[34] J. Stafford, E. Kendrick, Sustainable upcycling of spent electric vehicle anodes into solution-processable graphene nanomaterials, Ind. Eng. Chem. Res. 61 (44) (2022) 16529–16538, http://dx.doi.org/10.1021/acs.iecr.2c02634.

[35] C. Backes, K.R. Paton, D. Hanlon, S. Yuan, M.I. Katsnelson, J. Houston, R.J. Smith, D. McCloskey, J.F. Donegan, J.N. Coleman, Spectroscopic metrics allow in situ measurement of mean size and thickness of liquid-exfoliated few-layer graphene nanosheets, Nanoscale 8 (7) (2016) 4311–4323, http://dx.doi.org/10.1039/C5NR08047A.

[36] S. Marchesini, P. Turner, K.R. Paton, B.P. Reed, A.J. Pollard, Rapid monitoring of graphene exfoliation using NMR proton relaxation, Nanoscale 13 (34) (2021) 14518–14524, http://dx.doi.org/10.1039/D1NR03361A.

[37] C.R.K. Windows-Yule, J.P.K. Seville, A. Ingram, D.J. Parker, Positron emission particle tracking of granular flows, Annu. Rev. Chem. Biomol. Eng. 11 (1) (2020) 367–396, http://dx.doi.org/10.1146/annurev-chembioeng-011620-120633.

[38] K. Windows-Yule, L. Nicuşan, M.T. Herald, S. Manger, D. Parker, Positron Emission Particle Tracking – A Comprehensive Guide, IOP Publishing, Bristol, England, UK, 2022, http://dx.doi.org/10.1088/978-0-7503-3071-8.

[39] A.L. Nicuşan, C.R.K. Windows-Yule, Positron emission particle tracking using machine learning, Rev. Sci. Instrum. 91 (1) (2020) http://dx.doi.org/10.1063/1.5129251.

[40] M. Herald, T. Wheldon, C. Windows-Yule, Monte Carlo model validation of a detector system used for positron emission particle tracking, Nucl. Instrum. Methods Phys. Res. Sect. A 993 (2021) 165073, http://dx.doi.org/10.1016/j.nima.2021.165073.

[41] D.M. Hampel, S. Manger, D.J. Parker, T. Kokalova Wheldon, Superpept: A new tool for positron emission particle tracking; first results, Nucl. Instrum. Methods Phys. Res. A 1028 (2022) 166254, http://dx.doi.org/10.1016/j.nima.2021.166254.

[42] D. Dapelo, F. Alberini, J. Bridgeman, Euler-lagrange cfd modelling of unconfined gas mixing in anaerobic digestion, Water Res. 85 (2015) 497–511, http://dx.doi.org/10.1016/j.watres.2015.08.042.

[43] R.M. Ziff, E.D. McGrady, The kinetics of cluster fragmentation and depolymerisation, J. Phys. A: Math. Gen. 18 (15) (1985) 3027, http://dx.doi.org/10.1088/0305-4470/18/15/026.

[44] N.G. Özcan-Taşkin, G. Padron, A. Voelkel, Effect of particle type on the mechanisms of break up of nanoscale particle clusters, Chem. Eng. Res. Des. 87 (4) (2009) 468–473, http://dx.doi.org/10.1016/j.cherd.2008.12.012.

[45] J. Litster, Particle Size Reduction, Cambridge University Press, 2016, http://dx.doi.org/10.1017/CBO9781139017558.006.

[46] A.C. Ferrari, J.C. Meyer, V. Scardaci, C. Casiraghi, M. Lazzeri, F. Mauri, S. Piscanec, D. Jiang, K.S. Novoselov, S. Roth, A.K. Geim, Raman spectrum of graphene and graphene layers, Phys. Rev. Lett. 97 (18) (2006) 187401, http://dx.doi.org/10.1103/PhysRevLett.97.187401.

[47] G. Pagani, M.J. Green, P. Poulin, M. Pasquali, Competing mechanisms and scaling laws for carbon nanotube scission by ultrasonication, Proc. Natl. Acad. Sci. USA 109 (29) (2012) 11599–11604, http://dx.doi.org/10.1073/pnas.1200013109.

[48] B.N.J. Persson, On the fractal dimension of rough surfaces, Tribol. Lett. 54 (1) (2014) 99–106, http://dx.doi.org/10.1007/s11249-014-0313-4.

[49] L.W. Phipps, The fragmentation of oil drops in emulsions by a high-pressure homogenizer, J. Phys. D: Appl. Phys. 8 (4) (1975) 448, http://dx.doi.org/10.1088/0022-3727/8/4/018.

[50] S.S. Alves, J.M.T. Vasconcelos, J. Barata, Alternative compartment models of mixing in tall tanks agitated by multi-rushton turbines chem, Eng. Res. Des. 75 (3) (1997) 334–338, http://dx.doi.org/10.1205/026387697523642.